Annals of Nuclear Energy 111 (2018) 579–594

Contents lists available at ScienceDirect

Annals of Nuclear Energy

journal homepage: www.elsevier.com/locate/anucene

A Newton solution for the Superhomogenization method: The PJFNK-SPH

Javier Ortensi [a,*], Yaqi Wang [a], Alexandre Laurier [b], Sebastian Schunert [a], Alain Hébert [b], Mark DeHart [a]

[a] Idaho National Laboratory, 2525 N. Fremont Ave., Idaho Falls, ID 83401, USA
[b] École Polytechnique de Montréal, 2900 Boulevard Edouard-Montpetit, Montréal, QC H3T 1J4, Canada

ARTICLE INFO

Article history:
Received 16 May 2017
Received in revised form 6 September 2017
Accepted 15 September 2017

2017 MSC:
00-01
99-00

Keywords:
Superhomogenization
Equivalence
Homogenization
Rattlesnake
PJFNK
MOOSE

ABSTRACT

This work presents two novel topics regarding the Superhomogenization method: 1) the formalism for the implementation of the method with the linear Boltzmann Transport Equation, and 2) a Newton algorithm for the solution of the nonlinear problem that arises from the method. These new ideas have been implemented in a continuous finite element discretization in the MAMMOTH reactor physics application. The traditional solution strategy for this nonlinear problem uses a Picard, fixed-point iterative process whereas the new implementation relies on MOOSE's Preconditioned Jacobian-Free Newton Krylov method to allow for a direct solution. The PJFNK-SPH can converge problems that were either intractable or very difficult to converge with the traditional iterative approach, including geometries with reflectors and vacuum boundary conditions. This is partly due to the underlying Scalable Nonlinear Equations Solvers in PETSc, which are integral to MOOSE and offer Newton damping, line search and trust region methods. The PJFNK-SPH has been implemented and tested for various discretizations of the transport equation included in the Rattlesnake transport solver. Speedups of five times for diffusion and ten to fifteen times for transport were obtained when compared to the traditional Picard approach. The three test problems cover a wide range of applications including a standard Pressurized Water Reactor lattice with control rods, a Transient Reactor Test facility control rod supercell and a prototype fast-thermal reactor. The reference solutions and initial cross sections were obtained from the Serpent 2 Monte Carlo code. The SPH-corrected cross sections yield eigenvalues that are near exact, relative to reference solutions, for reflected geometries, even with reflector regions. In geometries with vacuum boundary conditions the accuracy is problem dependent and solutions can be within a few to a few hundred pcm. The root-mean-square error in the power distribution is below 0.8% of the reference Monte Carlo. There is little benefit from SPH-corrected transport in typical scoping calculations, but for more detailed analyses it can yield superior convergence of the solution in some of the test problems. This PJFNK-SPH approach is currently being used in the modeling of the Transient Test Reactor at Idaho National Laboratory, where full reactor core SPH-corrected cross sections are employed to reduce the homogenization errors in transient or multi-physics calculations. This base implementation of the PJFNK-SPH provides an extremely robust solver and a springboard to further improve the Superhomogenization method in order to better preserve neutron currents, one of the primary deficiencies of the method.

1. Introduction

Idaho National Laboratory (INL) has developed a high fidelity, strongly coupled multi-physics modeling capability under the Multi-physics Object Oriented Simulation Environment (MOOSE) framework (Gaston et al., 2009). MAMMOTH (Gleicher et al., 2014) is a MOOSE-based reactor physics application that couples Rattlesnake (radiation transport) (Wang, 2013), BISON (fuel performance) (Williamson et al., 2012), RELAP-7 (thermal-fluids) (Berry and Peterson, 2014), etc. Rattlesnake solves the steady-state, transient and k-eigenvalue problems for the multi-group radiation transport equations, the linear Boltzmann Transport Equation (BTE) discretized with the multigroup approximation for the energy variable. There are a number of different transport schemes available in Rattlesnake including self-adjoint angular flux (SAAF) formulation, the least squares formulation (LS) and the first order transport formulation. Rattlesnake also has a number of angular discretization schemes including spherical harmonics expansion (P_N), discrete ordinates (S_N) and diffusion.

* Corresponding author.
E-mail address: javier.ortensi@inl.gov (J. Ortensi).

https://doi.org/10.1016/j.anucene.2017.09.027
0306-4549/

There are continuous and discontinuous Finite Element Methods (FEM) for solving the P_N, S_N, and diffusion angular representation. Currently, the most tested and optimized solvers use the continuous FEM representation.

Most nuclear reactors are still too complex to allow high resolution modeling in every instance or there exist other constraints, e.g. run time for transient calculations, thus rendering detailed transport calculations infeasible. The method of choice for reducing the model complexity and allowing a reasonable representation without requiring too high a computational cost is the spatial homogenization of regions. Unfortunately, this spatial homogenization usually incurs errors that stem from the loss of information and fine details. There are currently two widely used homogenization techniques that aim to properly reproduce key quantities obtained from detailed computations of heterogeneous reactor regions. Both of these techniques are based on equivalence theory which states that, for each macro region in the homogenized reactor calculation, the averaged fluxes and reaction rates are to be in agreement with the heterogenous calculation. A literature search on various equivalence techniques can be found in the thesis that this work extends (Laurier, 2016).

The first method, expanding on equivalence theory, is called Generalized Equivalence Theory (GET) (Smith, 1986). Smith added another degree of freedom to the equations to allow the conservation of more than just averaged reaction rates and fluxes. This new parameter, called "discontinuity factor" (DF), allows for a better approximation of the neutron flux or currents at the boundaries. Although DFs produce good results in highly heterogeneous assemblies, the computational memory needed to do so is high, since a DF factor must be calculated and stored for every cell surface. Additionally, it requires a discontinuous method, which further demands evaluations at the cell surfaces. This heavy memory usage makes the use of DF difficult for three-dimensional pin-by-pin calculations. This equivalence procedure also has to explicitly take into account each discontinuity factor when solving the neutron transport equation over the full core whereas other methods allow for simpler modifications. A limiting aspect of this method arises from the availability of solvers with the capability of using discontinuous methods, which, as previously mentioned, are not yet well optimized within the Rattlesnake application.

The second widely used homogenization procedure, and the focus of this work, is called the Superhomogenisation (SPH) method. First described by Kavenoky et al. (1978) and later generalized by Hébert (1981), Hébert and Benoist (1991), Hébert (1993), Hébert and Mathonnière (1993), it introduces a new homogenization parameter, the SPH factor, to correct homogenized cross section errors. These SPH factors are applied to each averaged cross section to exactly reproduce the reaction rates from the heterogeneous calculation. Thus, for each macro region and energy group there is a unique SPH factor that is calculated, applied and does not need to be stored separately. This standard solution algorithm for obtaining the SPH factors is a fixed-point iterative method, which takes place between the main transport solver and the cross section modification step and does not require the modification of the already available full-core solvers to use SPH-corrected cross sections. One of the known shortcomings of the SPH method resides in its inability to conserve the neutron leakage. This is mainly due to the fact that the SPH method does not include enough degrees of freedom to preserve the currents between cells. A test illustrating this fact is included in Section 3.1.

In summary, the advantages of the SPH method over DFs are:

- simple implementation dealing with volumetric quantities,
- applicable to both continuous and discontinuous FEM,
- lower computational burden (no need to evaluate fluxes at the interfaces) and
- small data requirements (1 floating point per energy group per macro region).

The disadvantages of the SPH method over DFs are:

- does not produce an exact balance in geometries with reflectors or void boundary conditions and
- does not conserve currents (i.e. leakage) at the macro region interfaces.

Due to the need to implement an equivalence procedure in the continuous FEM solvers the SPH method is currently the best candidate. Since the transport systems in Rattlesnake are well modularized it was quite simple to implement the SPH procedure for a variety of solvers with minimal development effort. Therefore, the SPH procedure is now available in the continuous diffusion, SAAF-P_N and SAAF-S_N solvers.

The focus of this work is the preparation of SPH-corrected cross sections for transient simulations from complete analysis geometries and not in performing local lattice SPH corrections for assemblies in the traditional two-step analysis process (lattice-full core). This need is driven by the modeling and simulation of the Transient Reactor Test Facility (TREAT) (Ortensi et al., 2016) at INL. The current approach employs full core steady state Serpent Monte Carlo (Leppänen, 2015) models to generate cross sections. This is followed with Rattlesnake SPH calculations to prepare an SPH-corrected database later used in MAMMOTH transient simulations. Therefore, the principal interest of this work is to introduce the benefits of using a Newton Method for the SPH procedure and to investigate if there is a clear advantage to using SPH-corrected transport over SPH-corrected diffusion.

2. Methodology

2.1. The SPH equations

The Superhomogenisation (SPH) procedure is a cross section correction method that aims to preserve the reaction rates, leakage and eigenvalue within macro regions obtained through a homogeneous calculation with respect to a reference heterogeneous problem (Hébert, 1993). The correction is applied to reduce the error that originates from spatial homogenization, which modifies the physics of the problem. The SPH corrected cross sections are defined as the product of the reference cross section in macro region $m = 1, \ldots, M$ in energy group $g = 1, \ldots, G$ with its respective SPH factor $\mu_{m,g}$. There exists a unique SPH factor for each macro region m and energy group g such that the reaction rate in these regions is preserved:

$$\Sigma_{m,g} = \mu_{m,g}\Sigma^{ref}_{m,g} \tag{1}$$

In Eq. 1, the superscript "ref" represents the cross section value obtained using the condensation and homogenization process, but without applying the correction.

By definition of the SPH correction, the average reaction rate $\tau_{m,g}$ is to be preserved:

$$\tau^{ref}_{m,g} = \tau_{m,g} = \Sigma_{m,g}\phi_{m,g} = \Sigma^{ref}_{m,g}\phi^{ref}_{m,g} \tag{2}$$

where

$\phi^{ref}_{m,g}$ = reference heterogeneous flux in macro region m and group g

$\phi_{m,g}$ = homogeneous flux in macro region m and group g

$$\tau_{m,g} = \mu_{m,g}\Sigma^{ref}_{m,g}\phi_{m,g} = \Sigma^{ref}_{m,g}\phi^{ref}_{m,g} \tag{3}$$

from which the SPH factors are defined:

$$\mu_{m,g} = \frac{\phi^{ref}_{m,g}}{\phi_{m,g}}. \tag{4}$$

Eq. 3 shows that the flux $\phi_{m,g}$ depends on the value of the SPH factor. Therefore, $\mu_{m,g}$ and $\phi_{m,g}$ form a nonlinear system of equations:

$$\mu_{m,g} = \frac{\phi^{ref}_{m,g}}{\phi_{m,g}(\mu_{m,g})}. \tag{5}$$

The transport SPH problem entails a minimum of $M * G$ equations with $M * G$ unknowns (fluxes, and thus the SPH factors), which is the case for the diffusion approximation. It is easily found that an infinite number of scaled solutions of the fluxes satisfy the SPH equations. Therefore, a new scaling factor λ must be added to constrain the problem to a single set of solutions.

The traditional approach for λs is to define them in a way that preserves the domain averaged flux (flux-volume normalization) for each energy group g between the homogenized and reference lattice calculations (Hébert, 1993):

$$\sum_{m=1}^{M} \phi^{ref}_{m,g} V_m = \sum_{m=1}^{M} \lambda_g \phi_{m,g} V_m \tag{6}$$

$$\bar{\phi}^{ref}_g V_{tot} = \lambda_g \sum_{m \epsilon M} \phi_{m,g} V_m = \lambda_g \bar{\phi}_g V_{tot} \tag{7}$$

For this type of normalization, the sets of λ_g are thus defined as:

$$\lambda_g = \frac{\bar{\phi}^{ref}_g}{\bar{\phi}_g} \tag{8}$$

Applying this normalization to the macro fluxes, the first set of SPH factors that define a unique solution to the problem is defined as:

$$\mu_{m,g} = \frac{\phi^{ref}_{m,g}}{\phi_{m,g}} \frac{\bar{\phi}_g}{\bar{\phi}^{ref}_g} \tag{9}$$

Another approach for defining a unique set of SPH factors is to add a set of constraints to guarantee flux continuity between two different assemblies (Hébert and Mathonnière, 1993; Yamamoto et al., 2004). Following the logic behind the flux-volume normalization, the domain averaged flux is normalized to the reference boundary flux in each energy group. The normalization factors are then defined as:

$$\lambda_g = \frac{\phi^{ref}_g|_\partial}{\bar{\phi}_g} \tag{10}$$

where the notation $|_\partial$ is used to represent a value at the boundary of the problem. Applying this normalization to the fluxes, another unique set of SPH factors are defined:

$$\mu_{m,g} = \frac{\phi^{ref}_{m,g}}{\phi_{m,g}} \frac{\bar{\phi}_g}{\phi^{ref}_g|_\partial} \tag{11}$$

2.1.1. The SPH corrected neutron diffusion equation

To preserve the global reaction rate, the SPH corrected diffusion equation is (Hébert, 1993):

$$-\nabla \cdot \mu_{m,g} D_{m,g} \frac{\nabla \phi_g}{\mu_{m,g}} + \mu_{m,g} \Sigma_{m,g} \frac{\phi_g}{\mu_{m,g}} = \frac{\chi_g}{k_{eff}} \sum_{g'=1}^{G} \mu_{m,g'} \nu \Sigma_{f\,m,g'} \frac{\phi_{g'}}{\mu_{m,g'}} + \sum_{g' \neq g}^{G} \mu_{m,g'} \Sigma^{g \leftarrow g'}_{s,m} \frac{\phi_{g'}}{\mu_{m,g'}} \tag{12}$$

From the previous equation, the following rules are set for the SPH correction of the neutron diffusion equation:

- The diffusion coefficient $D_{m,g}$ and removal cross section $\Sigma_{m,g}$ are multiplied by $\mu_{m,g}$.
- The scattering $\Sigma^{g \leftarrow g'}_{s,m}$ and nu-fission $\nu\Sigma_{f,m,g'}$ cross section terms are multiplied by $\mu_{m,g'}$.

2.1.2. The SPH corrected neutron transport equation

Historically, the SPH method has been used with the neutron diffusion equation with satisfactory results. However, it is worth noting that diffusion theory is generally not applicable in most reactor regions and only the homogenization process makes the underlying approximations in diffusion theory valid. This is the case in mediums that strongly absorb neutrons, neutron scattering is strongly anisotropic, neutron streaming regions and in regions neighboring a neutron source or a material surface (within a few mean free paths).

Derivations of the SPH corrected neutron transport equations with the SP_N approximation have been proposed (Guerin et al., 2011; Hébert, 2015) but never tested. Chiba et al. (2012) corrected a 1-D mono-energetic transport equation and found the need to only preserve reaction rates computed with the P_0 and P_2 components of the angular flux.

The following derivation of the SPH corrected transport equation is presented with the P_N approximation since the summation notation is cleaner to work with than the integrals present in the classical transport equations. As such, the SPH corrected transport equations could have been derived using the integral notation or even through the S_N method. This means that the following derivation is also applicable for any transport scheme, including S_N, Simplified P_N (SP_N) and method of characteristics (MOC).

The even and odd equations of the multi-group neutron transport equation, treated with the P_N method, are used to describe the SPH correction:

$$even\ parity: \vec{\Omega} \cdot \vec{\nabla} \Psi^{odd}_g(\vec{x}, \vec{\Omega}) + \Sigma_{t,g}(\vec{x}) \Psi^{even}_g(\vec{x}, \vec{\Omega}) = \sum_{g'}^{G} \sum_{\ell}^{\infty}{}_{even} \frac{2\ell+1}{4\pi} \sum_{n=-\ell}^{\ell} \Sigma^{g \leftarrow g'}_{s,\ell}(\vec{x}) \phi_{g',\ell,n}(\vec{x}) Y_{\ell,n}(\vec{\Omega}) + \frac{\chi_g}{4\pi} \frac{1}{k_{eff}} \sum_{g'}^{G} \nu \Sigma_{f_{g'}}(\vec{x}) \phi_{g',0,0}(\vec{x}) \tag{13}$$

$$odd\ parity: \vec{\Omega} \cdot \vec{\nabla} \Psi^{even}_g(\vec{x}, \vec{\Omega}) + \Sigma^t_g(\vec{x}) \Psi^{odd}_g(\vec{x}, \vec{\Omega}) = \sum_{g'}^{G} \sum_{\ell}^{\infty}{}_{odd} \frac{2\ell+1}{4\pi} \sum_{n=-\ell}^{\ell} \Sigma^{g \leftarrow g'}_{s,\ell}(\vec{x}) \phi_{g',\ell,n}(\vec{x}) Y_{\ell,n}(\vec{\Omega}) \tag{14}$$

where

$Y_{\ell,n}(\vec{\Omega})$ are the spherical harmonics.

$\phi_{g,0,0}(\vec{x}) = \phi_g(\vec{x})$ represents the scalar flux.

and the even and odd parities of the flux are defined as:

$$\Psi^{even}_g(\vec{x}, \vec{\Omega}) = \frac{\left(\Psi_g(\vec{x}, \vec{\Omega}) + \Psi_g(\vec{x}, -\vec{\Omega})\right)}{2} \tag{15}$$

$$\Psi^{odd}_g(\vec{x}, \vec{\Omega}) = \frac{\left(\Psi_g(\vec{x}, \vec{\Omega}) - \Psi_g(\vec{x}, -\vec{\Omega})\right)}{2} \tag{16}$$

The scattering term $\phi_{g,\ell,n}$ is expanded in spherical harmonics $Y_{l,n}$ in the conventional form:

$$\int_{4\pi} d\Omega' \Sigma^g_x(\vec{x}, \vec{\Omega}', \vec{\Omega}) \Psi_g(\vec{x}, \vec{\Omega}') = \sum_{\ell=0}^{\infty} \frac{2\ell+1}{4\pi} \sum_{n=-\ell}^{\ell} \Sigma^g_{x,\ell}(\vec{x}) \phi_{g,\ell,n}(\vec{x}) Y_{\ell,n}(\vec{\Omega}) \tag{17}$$

The Eqs. 13 and 14 are now homogenized replacing the space variable $\vec{x}$ by the region index m, and the use of $\vec{\Omega}$ for denoting angular dependence of the variables is dropped:

$$even\ parity: \vec{\Omega}\cdot\vec{\nabla}\Psi_g^{odd} + \Sigma_{m,g}^t \Psi_g^{even} = \sum_{g'}^{G}\sum_{\ell}^{\infty}\sum_{even}\frac{2\ell+1}{4\pi}\sum_{n=-\ell}^{\ell}\Sigma_{s,\ell,m}^{g\leftarrow g'}\phi_{g',\ell,n}Y_{\ell,n} + \frac{\chi_g}{4\pi}\frac{1}{k_{eff}}\sum_{g'}^{G}\nu\Sigma_{f,g'}\phi_{g',0,0} \quad (18)$$

$$odd\ parity: \vec{\Omega}\cdot\vec{\nabla}\Psi_g^{even} + \Sigma_{m,g}^t \Psi_g^{odd} = \sum_{g'}^{G}\sum_{\ell}^{\infty}\sum_{odd}\frac{2\ell+1}{4\pi}\sum_{n=-\ell}^{\ell}\Sigma_{s,\ell,m}^{g\leftarrow g'}\phi_{g',\ell,n}Y_{\ell,n} \quad (19)$$

Eqs. 18 and 19 are now examined to determine the best way of applying the SPH factors. The goal of the SPH method is to preserve global reaction rates originating primarily from the zeroth (even) moment of the angular flux (Guerin et al., 2011). Using this fact, the SPH correction is first only applied to the cross sections and even fluxes that appear in the even equations. The cross sections are multiplied and the even fluxes divided by their respective SPH factors. There is no physical explanation as to why only the even flux moments are considered, but it has been discovered, through the course of this work, that preserving just the zeroth flux moment's contribution to the reaction rate does not allow for a valid SPH correction.

$$even\ parity: \vec{\Omega}\cdot\vec{\nabla}\Psi_g^{odd} + \mu_{m,g}\Sigma_{m,g}^t\frac{\Psi_g^{even}}{\mu_{m,g}} = \sum_{g'}^{G}\sum_{\ell}^{\infty}\sum_{even}\frac{2\ell+1}{4\pi}\sum_{n=-\ell}^{\ell}\mu_{m,g'}\Sigma_{s,\ell,m}^{g\leftarrow g'}\frac{\phi_{g',\ell,n}}{\mu_{m,g'}}Y_{\ell,n} + \frac{\chi_g}{4\pi}\times\frac{1}{k_{eff}}\sum_{g'}^{G}\mu_{m,g'}\nu\Sigma_{f,g'}\frac{\phi_{g',0,0}}{\mu_{m,g'}} \quad (20)$$

By preserving the contribution to the reaction rates from the even moments, all the even fluxes have to be divided by μ. This change also propagates to the odd equations which become:

$$odd\ parity: \vec{\Omega}\cdot\vec{\nabla}\frac{\Psi_g^{even}}{\mu_{m,g}} + \Sigma_{m,g}^t\Psi_g^{odd} = \sum_{g'}^{G}\sum_{\ell}^{\infty}\sum_{odd}\frac{2\ell+1}{4\pi}\sum_{n=-\ell}^{\ell}\Sigma_{s,\ell,m}^{g\leftarrow g'}\phi_{g',\ell,n}Y_{\ell,n} \quad (21)$$

At this point, only the cross sections in the even equations were modified. Since the correction does not yet apply to the cross sections in the odd equations, the reaction rate pertaining to these equations is no longer conserved. To do so, every other term of these equations must be divided by $\mu_{m,g}$:

$$odd\ parity: \vec{\Omega}\cdot\vec{\nabla}\frac{\Psi_g^{even}}{\mu_{m,g}} + \frac{1}{\mu_{m,g}}\Sigma_{m,g}^t\Psi_g^{odd} = \frac{1}{\mu_{m,g}}\sum_{g'}^{G}\sum_{\ell}^{\infty}\sum_{odd}\frac{2\ell+1}{4\pi}\sum_{n=-\ell}^{\ell}\Sigma_{s,\ell,m}^{g\leftarrow g'}\phi_{g',\ell,n}Y_{\ell,n} \quad (22)$$

Eqs. 20 and 22 correspond to the SPH corrected transport equations. At this point, the infinite sum over all moments must be truncated to a certain order N to allow for a numerical solution to the problem using spherical harmonics.

It is important to note that the total cross section in the even and odd equations are corrected differently; in the even Eq. 20 the total cross section is multiplied by μ whereas in the odd Eq. 22 the total cross section is divided by μ. This is because we cannot enforce conservation on both the even and odd moments of the angular flux at the same time. This may cause issues in solvers that do not differentiate between the moments of the total cross section, which is the case in Rattlesnake. In this case, a modification to the SPH corrected transport equations is needed to allow for a unique correction to the total cross section.

Another attempt at the derivation of the SPH neutron transport equation has been tried without success. Whereas the previous derivation had the reaction rates conserved within all the even transport equations, such as in Eq. 20, this other derivation demanded that only the zeroth moment of the reaction rate was preserved. This was accomplished by separating the zeroth moment of the flux from the rest of the even moments. Using the same derivation method used previously, a different SPH corrected transport equation was obtained which was tested to show that it did not preserve reaction rate. Since the primary source of reaction rate stems from the zeroth moments of the angular flux, there was no attempt to derive an SPH corrected transport equation where only the reaction rate stemming from the odd moments of the flux was preserved.

2.1.3. Modifying the total cross section

If a modification to the SPH corrected transport equations is in fact needed, we suggest two correction schemes which are mathematically equivalent and lead to very similar results in all cases studied. The first consists in having the total cross section multiplied by μ, in the fashion of the traditional SPH method. To do so, the following terms must be added to both sides of the odd SPH corrected transport Eqs. 22:

$$\mu_{m,g}\Sigma_{m,g}^t\Psi_g^{odd} - \frac{\Sigma_{m,g}^t\Psi_g^{odd}}{\mu_{m,g}} \quad (23)$$

to obtain:

$$odd\ parity: \vec{\Omega}\cdot\vec{\nabla}\frac{\Psi_g^{even}}{\mu_{m,g}} + \mu_{m,g}\Sigma_{m,g}^t\Psi_g^{odd} = \frac{1}{\mu_{m,g}}\sum_{g'}^{G}\sum_{\ell}^{N}\sum_{odd}\frac{2\ell+1}{4\pi}\sum_{n=-\ell}^{\ell}\Sigma_{s,\ell,m}^{g\leftarrow g'}\phi_{g',\ell,n}Y_{\ell,n} + \Sigma_{m,g}^t\Psi_g^{odd}\left(\mu_{m,g} - \frac{1}{\mu_{m,g}}\right) \quad (24)$$

The angular flux, Ψ_g^{odd}, on the right-hand side of the equation is expanded into its components:

$$odd\ parity: \vec{\Omega}\cdot\vec{\nabla}\frac{\Psi_g^{even}}{\mu_{m,g}} + \mu_{m,g}\Sigma_{m,g}^t\Psi_g^{odd} = \sum_{g'}^{G}\sum_{\ell}^{N}\sum_{odd}\frac{2\ell+1}{4\pi}\sum_{n=-\ell}^{\ell}\frac{\Sigma_{s,\ell,m}^{g\leftarrow g'}}{\mu_{m,g}}\phi_{g',\ell,n}Y_{\ell,n} + \sum_{\ell}^{N}\sum_{odd}\frac{2\ell+1}{4\pi}\sum_{n=-\ell}^{\ell}\Sigma_{m,g}^t(\mu_{m,g} - \frac{1}{\mu_{m,g}})\phi_{g',\ell,n}Y_{\ell,n} \quad (25)$$

and consolidate the last term into the scattering term using a Kronecker delta:

$$odd\ parity: \vec{\Omega}\cdot\vec{\nabla}\frac{\Psi_g^{even}}{\mu_{m,g}} + \mu_{m,g}\Sigma_{m,g}^t\Psi_g^{odd} = \sum_{g'}^{G}\sum_{\ell}^{N}\sum_{odd}\frac{2\ell+1}{4\pi}\sum_{n=-\ell}^{\ell}\left(\frac{\Sigma_{s,\ell,m}^{g\leftarrow g'}}{\mu_{m,g}} + \delta_{g,g'}\Sigma_{m,g}^t\left(\mu_{m,g} - \frac{1}{\mu_{m,g}}\right)\right)\phi_{g',\ell,n}Y_{\ell,n} \quad (26)$$

From the combination of the even (Eq. 20) and odd (Eq. 26), we get the following rules for the SPH correction for the neutron transport equation:

- The total cross section $\Sigma_{m,g}^t$ is multiplied by $\mu_{m,g}$.
- The nu-fission $\nu\Sigma_{f_{m,g'}}$ and ℓ even scattering $\Sigma_{s,\ell,m}^{g\leftarrow g'}$ cross section terms are multiplied by $\mu_{m,g'}$.

- for ℓ odd, the scattering cross section terms are corrected as:
$\Sigma^{g\leftarrow g'}_{s,\ell,m} \rightarrow \frac{\Sigma^{g\leftarrow g'}_{s,\ell,m}}{\mu_{m,g}} + \delta_{g,g'}\Sigma^{t}_{m,g}(\mu_{m,g} - \frac{1}{\mu_{m,g}})$.

2.1.4. Not modifying the total cross section

The second correction scheme suggested for the application of the SPH corrected transport equation relies on not modifying the total cross section. To do so, the same logic as in Section 2.1.3 is applied, where the following terms are added to the odd SPH corrected transport Eq. 22:

$$\Sigma^{t}_{m,g}\Psi^{odd}_{g} - \frac{\Sigma^{t}_{m,g}}{\mu_{m,g}}\Psi^{odd}_{g} \tag{27}$$

to obtain:

$$\begin{aligned} odd\ parity: \vec{\Omega}\cdot\vec{\nabla}\frac{\Psi^{even}_{g}}{\mu_{m,g}} + \Sigma^{t}_{m,g}\Psi^{odd}_{g} \\ = \frac{1}{\mu_{m,g}}\sum_{g'}^{G}\sum_{\ell\ odd}^{N}\frac{2\ell+1}{4\pi}\sum_{n=-\ell}^{\ell}\Sigma^{g\leftarrow g'}_{s,\ell,m}\phi_{g',\ell,n}Y_{\ell,n} \\ + \Sigma^{t}_{m,g}\Psi^{odd}_{g}\left(1-\frac{1}{\mu_{m,g}}\right) \end{aligned} \tag{28}$$

Since the total cross section is no longer modified, the even Eq. 20 must also be changed:

$$\begin{aligned} even\ parity: \vec{\Omega}\cdot\vec{\nabla}\Psi^{odd}_{g} + \Sigma^{t}_{m,g}\frac{\Psi^{even}_{g}}{\mu_{m,g}} \\ = \sum_{g'}^{G}\sum_{\ell\ even}^{N}\frac{2\ell+1}{4\pi}\sum_{n=-\ell}^{\ell}\mu_{m,g'}\Sigma^{g\leftarrow g'}_{s,\ell,m}\frac{\phi_{g',\ell,n}}{\mu_{m,g'}}Y_{\ell,n} \\ + \frac{\chi_g}{4\pi}\frac{1}{k_{eff}}\sum_{g'}^{G}\mu_{m,g'}\nu\Sigma_{f_{g'}}\frac{\phi_{g'}}{\mu_{m,g'}} + \Sigma^{t}_{m,g}\frac{\Psi^{even}_{g}}{\mu_{m,g}}\left(1-\mu_{m,g}\right) \end{aligned} \tag{29}$$

where Ψ^{even}_{g} and Ψ^{odd}_{g} in the previous equations are now expanded in their components and consolidated into the scattering term:

$$\begin{aligned} even\ parity: \vec{\Omega}\cdot\vec{\nabla}\Psi^{odd}_{g} + \Sigma^{t}_{m,g}\frac{\Psi^{even}_{g}}{\mu_{m,g}} \\ = \sum_{g'}^{G}\sum_{\ell\ even}^{N}\frac{2\ell+1}{4\pi}\sum_{n=-\ell}^{\ell}\left(\mu_{m,g'}\Sigma^{g\leftarrow g'}_{s,\ell,m} + \delta_{g,g'}\Sigma^{t}_{m,g}(1-\mu_{m,g})\right)\frac{\phi_{g',\ell,n}}{\mu_{m,g'}}Y_{\ell,n} \\ + \frac{1}{k_{eff}}\frac{\chi_g}{4\pi}\sum_{g'}^{G}\mu_{m,g'}\nu\Sigma_{f_{m,g'}}\frac{\phi_{g'}}{\mu_{m,g'}} \end{aligned} \tag{30}$$

$$\begin{aligned} odd\ parity: \vec{\Omega}\cdot\vec{\nabla}\frac{\Psi^{even}_{g}}{\mu_{m,g}} + \Sigma^{t}_{m,g}\Psi^{odd}_{g} \\ = \sum_{g'}^{G}\sum_{\ell\ odd}^{N}\frac{2\ell+1}{4\pi}\sum_{n=-\ell}^{\ell}\left(\frac{\Sigma^{g\leftarrow g'}_{s,\ell,m}}{\mu_{m,g}} + \delta_{g,g'}\Sigma^{t}_{m,g}(1-\frac{1}{\mu_{m,g}})\right)\phi_{g',\ell,n}Y_{\ell,n} \end{aligned} \tag{31}$$

This correction scheme does not modify the total cross sections, and the correction required by the equivalence relations are transferred to the scattering terms. These two methods of cross section corrections are mathematically equivalent, assuming a summation over infinite values of N. The cross sections are corrected following these rules:

- The total cross section $\Sigma^{t}_{m,g}$ is not modified.
- The fission cross section $\nu\Sigma_{f_{m,g'}}$ is multiplied by $\mu_{m,g'}$.
- for ℓ even, the scattering cross section terms are corrected as:
$\Sigma^{g\leftarrow g'}_{s,\ell,m} \rightarrow \mu_{m,g'}\Sigma^{g\leftarrow g'}_{s,\ell,m} + \delta_{g,g'}\Sigma^{t}_{m,g}(1-\mu_{m,g})$.
- for ℓ odd, the scattering cross section terms are corrected as:
$\Sigma^{g\leftarrow g'}_{s,\ell,m} \rightarrow \frac{\Sigma^{g\leftarrow g'}_{s,\ell,m}}{\mu_{m,g}} + \delta_{g,g'}\Sigma^{t}_{m,g}(1-\frac{1}{\mu_{m,g}})$..

2.2. Solution strategies

The SPH factors are determined from the solution of the nonlinear system of the SPH equations. For simplicity, the process of obtaining the SPH factors is only explained via the diffusion equation in this work, since the method is the same with the transport operator. Two iterative solution strategies are discussed: the first approach is the traditional SPH iteration, which relies on a fixed-point iterative process of linear system solutions; the second and novel approach, named PJFNK-SPH method, relies on the Preconditioned Jacobian-Free Newton Krylov method (Knoll and Keyes, 2004).

2.2.1. The traditional SPH iteration

The traditional approach to solving for the SPH factors relies on a Picard, fixed-point, iterative process (Fujita et al., 2015; Yamamoto et al., 2004; Chiba et al., 2012; Hébert, 2015; Guerin et al., 2011; Li et al., 2014; Grundmann and Mittag, 2011; Nikitin et al., 2015; Ma et al., 2015). The neutron diffusion equation with SPH corrected cross sections takes the form:

$$\begin{aligned} -\nabla\cdot\mu_{m,g}D_{m,g}\nabla\phi_g + \mu_{m,g}\Sigma_{m,g}\phi_g \\ = \frac{\chi_g}{k_{eff}}\sum_{g'=1}^{G}\mu_{m,g'}\nu\Sigma_{f\,m,g'}\phi_{g'}\lambda_{g'} + \sum_{g'\neq g}^{G}\mu_{m,g'}\Sigma^{g\leftarrow g'}_{s,m}\phi_{g'}\lambda_{g'} \end{aligned} \tag{32}$$

The SPH procedure consists of Algorithm 1:

Algorithm 1. Traditional SPH

Data: cross sections, k_{eff}, χ_g and reference fluxes $\phi^{ref}_{m,g}$ from a reference calculation.

Initialization: $\mu^{(0)}_{m,g} = 1$ and $\phi^{ref}_{m,g}$ is used to build the source;

while *cond1* **do**

(-nonlinear iteration- k indexing)

1. The SPH factors are applied to the cross sections.
2. Build the source term of Eqn. 32 with the flux solution ϕ^{k}_{g}.
3. Solve for ϕ^{k+1}_{g} by inverting the left-hand side of Eqn. 32.
(-linear iteration-)
4. Recalculate the macro-region fluxes $\phi^{k+1}_{m,g}$ and $\mu^{k+1}_{m,g}$ with Eqn. 5.

end

---

where *cond*1 is

$$\frac{|\mu^{(k+1)}_{m,g} - \mu^{(k)}_{m,g}|}{\mu^{(k+1)}_{m,g}} > \epsilon_{\mu} \tag{33}$$

and ϵ_{μ} is usually taken to be smaller than 10^{-4}.

2.2.2. Preconditioned Jacobian-Free Newton Krylov SPH method

The MOOSE framework uses a Preconditioned Jacobian-Free Newton Krylov (PJFNK) (Knoll and Keyes, 2004) method as the default option to solve nonlinear problems.

The Jacobian-Free Newton Krylov (JFNK) method is a fully-coupled, multi-level algorithm for solving large nonlinear equation systems. In the case of MOOSE, it consists of two levels: an outer

Newton loop for the nonlinear solve and an inner Krylov loop for the linear system of equations that arises within each Newton iteration (Berry and Peterson, 2014). The notation used for the system of equations is:

$$\boldsymbol{F}(\boldsymbol{u}) = 0 \tag{34}$$

where $\boldsymbol{u}$ are the scalar fluxes. At the k^{th} iteration, the residual vector $\boldsymbol{r}^k$, which is to be minimized, is defined as:

$$\boldsymbol{r}^k \equiv \boldsymbol{F}(\boldsymbol{u}^k) \tag{35}$$

To update the solution vector, the following equation must be solved for the change vector $\delta\boldsymbol{u}^k = \boldsymbol{u}^{k+1} - \boldsymbol{u}^k$:

$$\boldsymbol{J}(\boldsymbol{u}^k)\delta\boldsymbol{u}^k = -\boldsymbol{r}^k \tag{36}$$

where $\boldsymbol{J}(\boldsymbol{u}^k)$ is the Jacobian matrix evaluated at $\boldsymbol{u}^k$:

$$J_{ij} \equiv \frac{\partial F_i}{\partial u_j} \tag{37}$$

After $\delta\boldsymbol{u}^k$ is calculated, the next value of the vector solution is:

$$\boldsymbol{u}^{k+1} = \boldsymbol{u}^k + \delta\boldsymbol{u}^k \tag{38}$$

In MOOSE, this Newton iteration is completed when the residual vector norm $|\boldsymbol{r}^k|$ or the relative residual vector norm between two iterations meet the convergence criteria. The system of equations presented in Eq. 36 is a very large problem set. However, in the JFNK method, the Jacobian matrix does not need to be fully assembled and the matrix–vector product is approximated by the finite difference form

$$\boldsymbol{J}\boldsymbol{v} \approx \frac{\boldsymbol{F}(\boldsymbol{u}^k + \epsilon\boldsymbol{v}) - \boldsymbol{F}(\boldsymbol{u}^k)}{\epsilon}. \tag{39}$$

where

ϵ is the perturbation parameter and,
$\boldsymbol{v}$ is provided by the Krylov method.

Strong preconditioning is required for Krylov methods to be efficient, or else the convergence is very slow. Using right preconditioning as an example, Eq. 36 can be transformed to:

$$\boldsymbol{J}^k\boldsymbol{P}^{-1}\left(\boldsymbol{P}\delta\boldsymbol{u}^k\right) = -\boldsymbol{r}^k \tag{40}$$

where $\boldsymbol{P}$ is a preconditioning matrix. The preconditioned Krylov iterations require the additional operation $P^{-1}\boldsymbol{v}$ and are solved in PETSc with one of the supported methods, of which, Algebraic Multi-Grid (AMG) is normally used. This preconditioning matrix is a simpler form of the original Jacobian matrix $\boldsymbol{J}$. For neutron transport the preconditioning matrix is currently built without the off-diagonal scattering terms and ignoring the flux dependence of the SPH factors.

The PJFNK-SPH method is very similar to the iterative SPH process. The main difference arises in the solution of the linear system, which is updated with the latest iterate of the solution vector after each linear residual evaluation. A second difference is the test for convergence. While the convergence test in the traditional SPH iteration is performed on the SPH factors themselves, in the PJFNK-SPH the convergence test is performed on the residual vector $\boldsymbol{r}^k$, which contains the fluxes. The details of the PJFNK-SPH method are delineated in Algorithm 2. In the new method, the converged solution can be obtained in a fraction of the time due to the frequent update of the linear system. It is also very robust as long as the initial guess is within the radius of convergence of the Newton Method, and is not an issue for simple SPH problems. For more complex problems, such as those with very large reflector regions or void boundary conditions, the initial guess can be forced within the radius of convergence of the Newton Method with a few traditional SPH iterations. This initial update is referred herein as a *free SPH iteration*.

Additionally, the MOOSE capabilities are built on PETSc, which contains the Scalable Nonlinear Equations Solvers (SNES) and offers Newton damping, line search and trust region methods. In Newton damping, a damping factor α between 0 and 1 is introduced to Eq. 38 in order to limit the extrapolation with

$$\boldsymbol{u}^{k+1} = \boldsymbol{u}^k + \alpha\delta\boldsymbol{u}^k. \tag{41}$$

The dampened Newton method leads to slower convergence of the solution but is less sensitive to bad initial guesses.

Algorithm 2. PJFNK-SPH

Data: cross sections, k_{eff}, χ_g and fluxes $\phi^{ref}_{m,g}$ from a reference calculation.
Initialization: $\mu^{(0)}_{m,g} = 1$ and $\phi^{ref}_{m,g}$ is used to build the source;
while *cond2 and cond3* **do**
(-nonlinear iteration- k indexing)
1. Apply SPH factors to the cross sections.
2. Perform a residual evaluation $\boldsymbol{F}(\boldsymbol{u}^k)$.
3. Solve for $\delta\boldsymbol{u}^k$ in Eqn. 36 with Krylov method.
while *cond4* **do**
(-linear iteration- j indexing)
(a) Apply SPH factors to the cross sections.
(b) Perform a linear residual evaluation $\boldsymbol{r}^{j+1} = \boldsymbol{F}(\boldsymbol{u}^k + \epsilon\boldsymbol{v})$.
(c) Recalculate the macro-region fluxes $\phi^{j+1}_{m,g}$ and SPH factors $\mu^{j+1}_{m,g}$ with the next flux iterate $\boldsymbol{v}^{j+1}$.
end
4. Update flux vector solution with Eqn. 38.
5. Recalculate the macro-region fluxes $\phi^{k+1}_{m,g}$ and $\mu^{k+1}_{m,g}$ with Eqn. 5.
end

where:

$$cond2: \|\boldsymbol{r}_{nl}\|_2 > \epsilon_{nl} \qquad cond3: \frac{\|\boldsymbol{r}_{nl}\|_2}{\|\boldsymbol{r}^0_{nl}\|_2} > \epsilon_{nl} \qquad cond4: \frac{\|\boldsymbol{r}_l\|_2}{\|\boldsymbol{r}^0_l\|_2} > \epsilon_l$$

ϵ_{nl} is the absolute tolerance for the nonlinear iteration,
ϵ^r_{nl} is the relative tolerance for the nonlinear iteration,
ϵ^r_l is the relative tolerance for the linear iteration,
$\|\boldsymbol{r}^0_{nl}\|_2$ is the initial l2 norm for the nonlinear iteration.

2.2.3. Comparison of methods

In order to compare the runtime for the two solution strategies, it is necessary to set similar convergence criteria. This is accomplished by first obtaining the PJFNK-SPH solution and computing a SPH factor convergence tolerance with

$$\epsilon = max\left\{\frac{|\mu^{(k+1)}_{m,g} - \mu^{(k)}_{m,g}|}{\mu^{(k+1)}_{m,g}}\right\}. \tag{42}$$

This new tolerance is used in the traditional SPH iteration using one nonlinear iteration, thus forcing only linear solutions to the system at each SPH iteration. The SPH algorithm will not exit until the SPH factors are converged within this tolerance.

3. Test problems

The purpose of the test problems is to study the convergence characteristics and accuracy of the PJFNK-SPH method for diffusion and transport solvers in various reactor types. The four analyzed

test problems are: 1) leakage test, 2) a 2-D PWR lattice, 3) 3-D TREAT supercell, 4) 2-D Coupled Test Reactor.

All reference solutions and cross sections were obtained with the continuous energy Monte Carlo code Serpent 2 (Leppänen, 2015) using ENDF/B-VII.1-based data. The homogenized cross sections from the Serpent output we converted to the YAKXS XML format used in Rattlesnake. The energy group structures used in the analyses are included in Table 1.

3.1. SPH leakage test

A test problem shown in Fig. 1 is used to illustrate the limitations of the SPH method with regard to the preservation of the leakage. This test involves a 3 × 3 PWR fuel pin arrangement with reflected boundary conditions. Two different enrichment zones are used: 1) a high enrichment zone in locations 1 to 2 and 2) a low enrichment zone in locations 3–9. The cross sections are condensed to the four group structure shown in Table 1.

Table 1
Upper Energy Boundaries (eV).

Group	*11-group*	*9-group*	*8-group*	*4-group*
1	1.000E+43	1.000E+43	1.000E+43	1.000E+43
2	3.329E+06	2.231E+06	7.065E+05	8.210E+05
3	1.156E+05	3.020E+05	5.005E+03	5.530E+03
4	3.481E+03	4.087E+04	4.000E+00	6.250E−01
5	1.327E+02	9.119E+03	6.250E−01	
6	8.100E+00	1.234E+03	2.800E−01	
7	6.250E−01	1.486E+02	1.380E−01	
8	2.096E−01	2.260E+01	5.550E−02	
9	7.650E−02	4.000E+00		
10	4.730E−02			
11	2.001E−02			

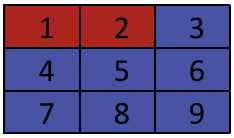

Fig. 1. SPH leakage test problem.

3.2. Pressurized water reactor assembly

The SPH method is known to work well for PWR assemblies and the second problem consists of a 17 × 17 PWR assembly defined in the BEAVRS benchmark (Horelik et al., 2013). An assembly containing strong absorbers in the form of control rods is homogenized into 9 flat cross section regions, as shown in Fig. 2. The 17x17 assembly in Fig. 2b is composed of fuel pin cells (regions 1–10), instrumentation tube cell (region 12), control rod cells (region 13), and the surrounding water gap beyond the grid. The grouping of these cells is based on the type of pin (fuel pin, control rods, etc.) and on their immediate neighbors. The symmetry of the problem is also taken into account during the homogenization process. In the reference calculation, each fuel pin is modeled according to the BEAVRS benchmark specifications with full heterogeneity to define the various pins. The energy spectrum was condensed to the *8-group* structure in Table 1 for each of the flat cross section regions. The assembly used in the analysis contains 3.1% enrichment fuel. The analysis base mesh uses a single QUAD4 element for each pin-cell.

3.3. TREAT control rod

This problem consists of a 3 by 3 supercell problem, shown in Figs. 3 and 4, with a control rod fuel element positioned in the center and surrounded by standard fuel elements. The cross sections obtained from the Serpent model are fully homogenized in the radial direction within each fuel element with 13 axial locations to capture reflector effects. The energy spectrum was condensed to the *11-group* structure in Table 1 for each of the flat cross section regions. Furthermore, the cross sections for the face and diagonally adjacent standard elements are segregated in order to better model the geometry. This supercell includes axial graphite reflectors on top and bottom of the active core, where a vacuum boundary is imposed.

3.4. Coupled test reactor

The coupled test reactor is envisioned as a thermal-fast irradiation prototype (Youinou et al., 2016) under development at INL. The center positions contain fast reactor fuel and fast test zones, while the outer positions contain the thermal fuel and thermal test zones (see Fig. 5). This 2-D model does not contain axial blankets. The base mesh uses a wedge element (extruded triangle) that con-

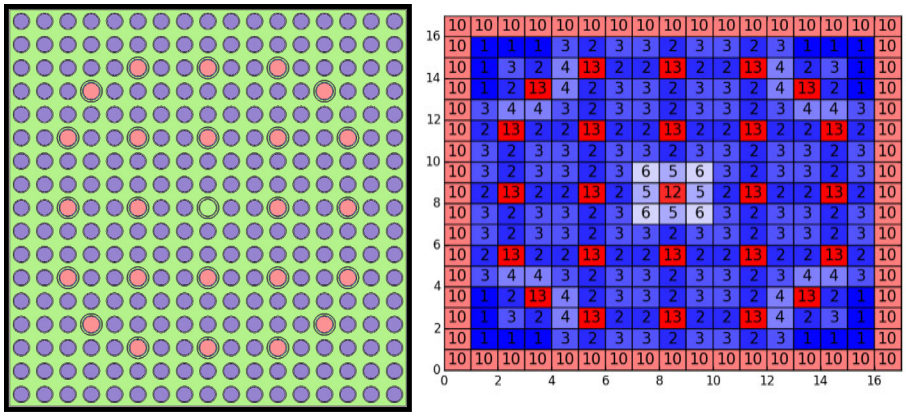

(a) Serpent (b) MAMMOTH flat cross section regions

Fig. 2. Geometry and region assignment for the PWR lattice.

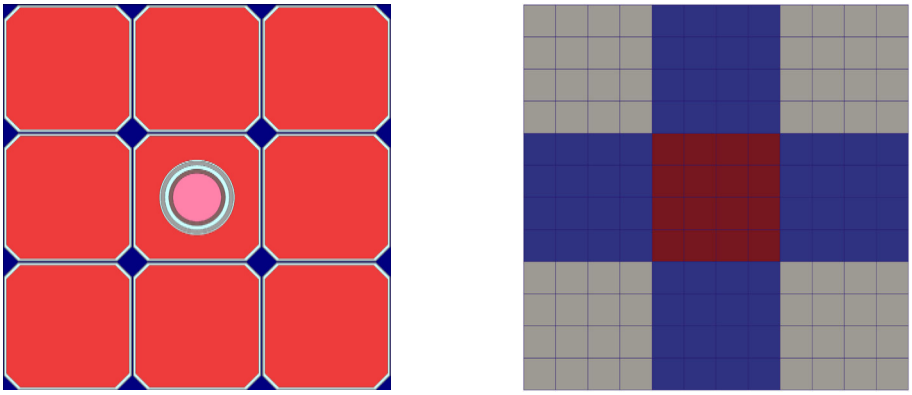

(a) Serpent (b) MAMMOTH Mesh

Fig. 3. X-Y plane geometry and mesh for the 3 × 3 supercell. B_4C poison region shown in pink.

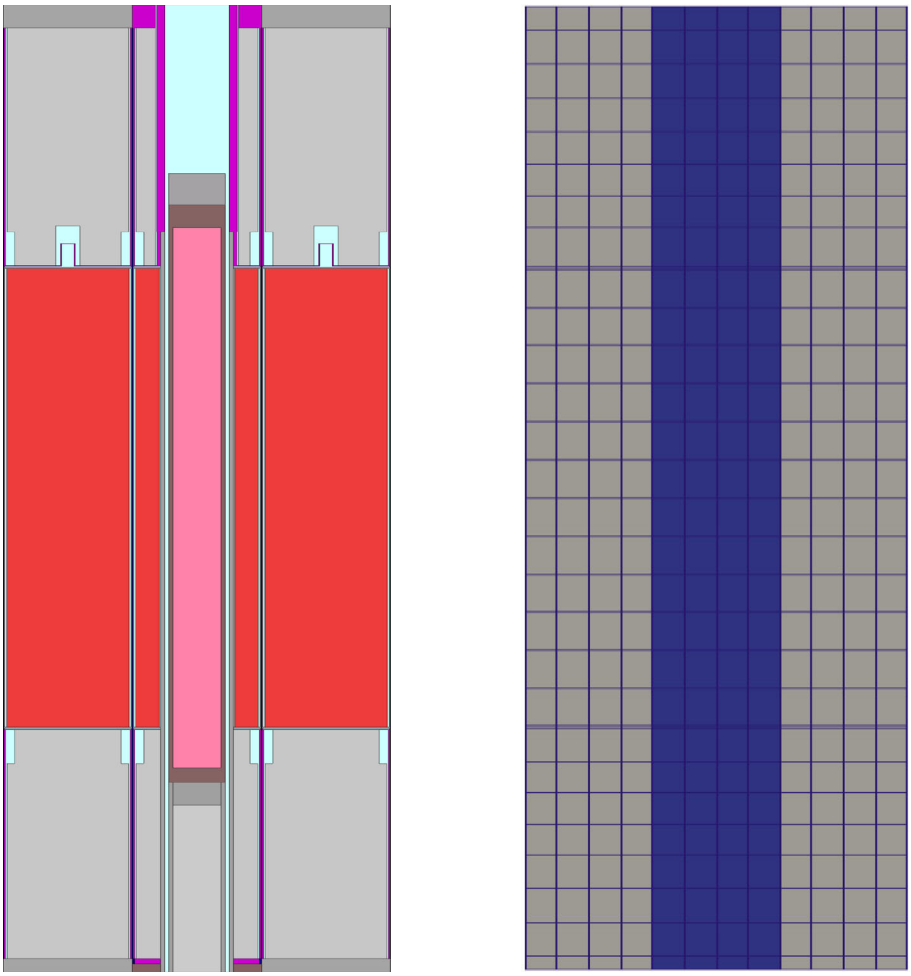

(a) Serpent (b) MAMMOTH Mesh

Fig. 4. X-Z plane geometry and mesh for the 3 × 3 supercell.

stitutes 1/6th of each hexagon. This reactor poses the challenge of including separate fast and thermal neutron zones, reflectors, neutron filters, and void boundary conditions. In this problem the energy spectrum was condensed to the *9-group* structure in Table 1 for each of the flat cross section regions.

4. Results

A number of convergence studies were conducted on the SPH correction for the diffusion and transport solvers. In these studies

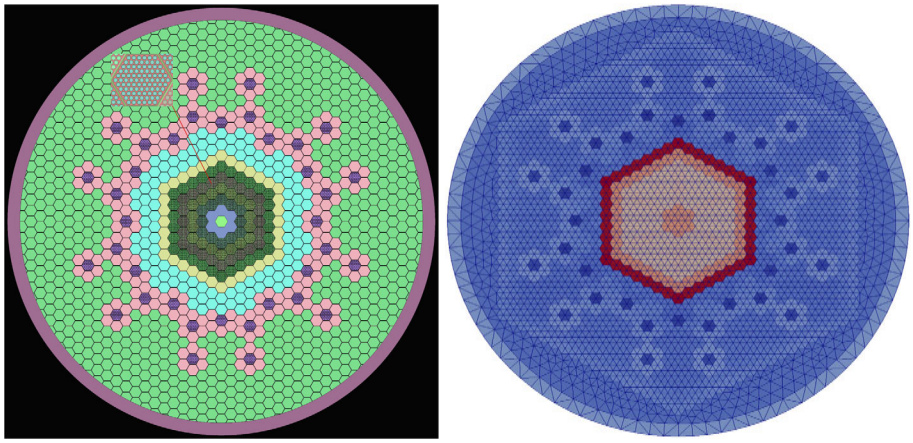

(a) Serpent (b) MAMMOTH Mesh

Fig. 5. Coupled Test Reactor Model.

Table 2
Percent relative error in the net current for each energy group.

Discretization	surface	g1	g2	g3	g4
Diffusion	1–2	16.6%	4.6%	17.7%	12.2%
P_7	1–2	-12.4%	-2.5%	-9.8%	2.9%
Diffusion	1–4	-41.2%	-38.9%	-44.1%	-41.0%
P_7	1–4	-9.9%	-7.9%	-17.2%	-16.2%

Table 3
Solutions to the PWR lattice problem.

Discretization	h	p	Eigenvalue	pcm
Diffusion (no SPH)	1	2	0.76060	-7399.8
P_{17} (l = 2) (no SPH)	1	2	0.79687	-2984.1

both calculations with the SPH-corrected cross sections and iterative SPH solutions employ identical models (spatial, angular and scattering discretization). The SPH correction can be particularly sensitive to the spatial, angular and scattering discretization that was used in the SPH iteration for highly heterogeneous media. Both mesh (h-refinement) and polynomial (p-refinement) spatial refinement are employed. The h-refinement is based on a uniform refinement approach. For a quadrilateral element in 2-D, this implies that h-refinement 0, 1, 2, 3 leads to 1, 4, 16 and 64 elements. Furthermore, there is no scattering source truncation for the transport methods where the l index refers to the order of the scattering data available in the cross section library. With regard to the total cross section correction in transport SPH, the default approach is not to modify the total cross section, as delineated in Section 2.1.4. Several Figures-of-Merit (FOM) for the percent relative difference between the MAMMOTH and reference Monte Carlo are used to assess the accuracy of the solutions. These include the root-mean-square (RMS), maximum (max), minimum (min) and the range.

4.1. SPH leakage test

Both SPH corrected diffusion and P_7 preserve the eigenvalue and the average fluxes in each cell exactly. The evaluation of the net currents at two cell interfaces is shown in Table 2. The P_7

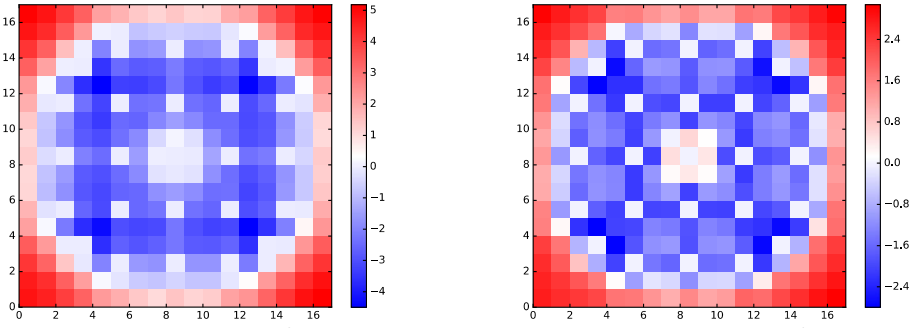

(a) Diffusion (b) P_{17}

Fig. 6. % rel. diff. in the power distribution for the PWR lattice - no SPH.

SPH solution yields better estimates of the net current over diffusion but still fails to exactly preserve this quantity with significant errors between 8 to 18%.

4.2. Pressurized water reactor lattice

The eigenvalues for diffusion and P_{17} without SPH correction are shown in Table 3. These represent well converged solutions and were obtained with one level of uniform h-refinement and second-order Lagrange polynomial order. Due to the presence of control rods the homogenization error is rather large ($\gtrsim$ 3,000 pcm). The percent relative difference in the power distribution compared to Monte Carlo is included in Fig. 6. Both solutions underpredict the local pin-cell power near the control rods and overpredict the power in pin-cells near the lattice corners. The range of the relative difference for diffusion is 9.68% and 5.87% for transport.

The eigenvalues obtained with SPH corrected cross sections always reproduce the reference (~4 pcm), since reflected boundary conditions are imposed on all boundaries. The h-refinement study shown in Table 4 suggests that the diffusion solution produces better results with 0 refinement than P_5 transport, but the P_N method experiences a large improvement with the first uniform refinement, 44% and 62% improvement in the RMS, respectively. After the first refinement the improvements in the power distribution are less important. The same trend is observed for p-refinement in Table 5. This type of refinements is preferred, since in FEM it produces higher order spatial convergence, thus 2nd order p-refinement leads to better solutions than any h-refinement in Table 4. The limiting factor in larger CFEM simulations is the size of the connectivity matrix, which can dramatically increase memory requirements. The transport solution with this higher spatial refinement leads to improved solutions over diffusion, but the benefits are small due to the cost of the P_5 calculation.

A P_N order convergence study in Table 6 indicates that the P_5 solution is already well converged and marginal gains are realized from using more angular moments in the SPH correction.

Finally, the convergence of the scattering order in Table 7 shows that there is no benefit from higher order scattering beyond linear anisotropic. The corrections of the isotropic scattering matrix are not sufficient to preserve the neutron balance and the linear anisotropic matrix is necessary for this problem and, incidentally, for most thermal reactor problems with SPH corrected transport.

When comparing the Picard and PJFNK-SPH strategies for computing SPH factors the superior performance of PJFNK-SPH is evident in Table 8. Very large improvements in the run-time are observed for the larger problems with factors of 10 and higher. Factors of 5 are seen in the diffusion solutions.

The effects of the SPH correction on the power distribution are illustrated in Fig. 7. The diffusion solution is shown in Fig. 7(a), whereas the difference between diffusion and SPH-diffusion is found in Fig. 7(b). The results show that the power is overpredicted near the control rod locations and underpredicted in the assembly corners.

4.3. TREAT control rod supercell

The TREAT control rod supercell model includes reflectors and void boundary conditions. The results from a spatial discretization study with diffusion are included in Table 9. The SPH correction provides a substantial improvement in the eigenvalue and power distribution. The SPH eigenvalues are within ~300 pcm of the reference Monte Carlo, whereas the uncorrected prediction is ~5,700 pcm from the reference. The improvement in the RMS power is roughly a factor of 9. Further discretization of the SPH solution appears to improve the eigenvalue prediction whilst the accuracy of the power prediction degrades. This can arise from better convergence of the solution. It is worth noting that the eigenvalue is not strictly preserved since the method does not preserve the currents and is primarily due to the imposition of the void boundary

Table 4
Effects of SPH correction h-refinement on power distribution.

Discretization	h	rms	max	min	range
Diffusion SPH	0	0.345	1.263	-1.212	2.475
	1	0.195	0.760	-0.512	1.272
	2	0.169	0.655	-0.436	1.091
	3	0.164	0.637	-0.425	1.062
P_5 SPH	0	0.476	1.316	-3.104	4.420
(l = 1)	1	0.181	0.760	-0.737	1.497
	2	0.166	0.664	-0.520	1.184
	3	0.165	0.639	-0.532	1.171

Table 5
Effects of p-refinement of the SPH correction on power distribution.

Discretization	p	rms	max	min	range
Diffusion SPH	1	0.345	1.263	-1.212	2.475
	2	0.161	0.637	-0.407	1.045
P_5 SPH	1	0.476	1.316	-3.104	4.420
(l = 1)	2	0.146	0.581	-0.445	1.026

Table 6
Effects of angular convergence of the SPH correction on power distribution (h0p2).

Discretization	rms	max	min	range
P_1 (l = 1)	0.183	0.837	-0.624	1.461
P_3 (l = 1)	0.153	0.600	-0.483	1.083
P_5 (l = 1)	0.146	0.581	-0.445	1.026
P_7 (l = 1)	0.143	0.580	-0.432	1.012

Table 7
Effects of scattering order convergence of the SPH correction on power distribution (P_5, h0p2).

scattering order	rms	max	min	range
0	2.291	6.067	-4.763	10.830
1	0.146	0.581	-0.445	1.026
2	0.153	0.611	-0.443	1.053
3	0.153	0.611	-0.443	1.053
4	0.153	0.611	-0.443	1.053

Table 8
Comparison between traditional and PJFNK-SPH for a PWR lattice.

Discretization	SPH Solver	# Iterations	CPU Time [sec]	Speed Up
Diffusion	traditional	32	45.10	-
	PJFNK-SPH	4	7.85	5.74
P_1	traditional	25	94.58	-
	PJFNK-SPH	3	19.80	4.78
P_3	traditional	30	602.21	-
	PJFNK-SPH	3	69.42	8.68
P_5	traditional	30	1734.04	-
	PJFNK-SPH	3	182.71	9.49
S_2	traditional	73	360.15	-
	PJFNK-SPH	4	33.00	10.91
S_4	traditional	70	1008.54	-
	PJFNK-SPH	4	75.30	13.39
S_6	traditional	72	2629.34	-
	PJFNK-SPH	4	179.31	14.66

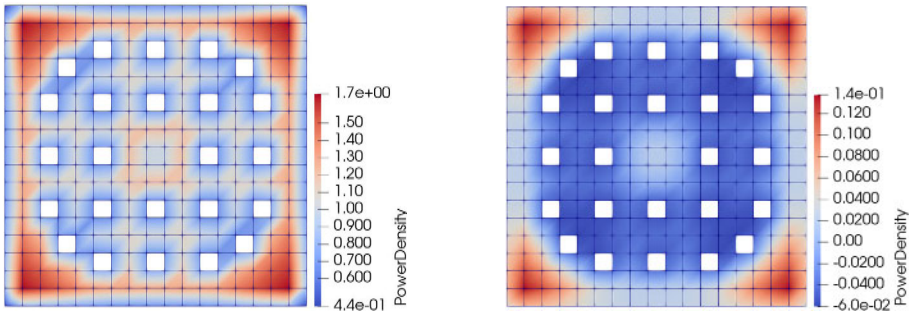

(a) Diffusion values (b) SPH-Correction

Fig. 7. SPH-correction of the power density in the PWR lattice (h0p1).

Table 9
Diffusion solutions for the TREAT 3 × 3 with void axial boundary conditions.

Discretization	h	p	Eigenvalue	pcm	rms	max	min	range
Ref.	-	-	0.673196	(±2.2)	–	–	–	–
Diffusion	0	1	0.630806	-6296.8	4.832	14.660	-2.405	17.065
(no SPH)	1	1	0.633826	-5848.2	4.567	13.831	-3.099	16.93
	0	2	0.634830	-5699.1	4.485	13.582	-3.320	16.902
Diffusion SPH	0	1	0.675743	378.4	0.319	0.842	-0.601	1.443
	1	1	0.675326	316.3	0.439	0.462	-1.239	1.701
	0	2	0.675192	296.5	0.522	0.534	-1.429	1.963

Table 10
Diffusion solutions for the TREAT 3 × 3 with reflected axial boundary conditions.

Discretization	h	p	Eigenvalue	pcm	rms	max	min	range
Ref.	-	-	0.674472	(±2.2)	–	–	–	–
Diffusion	0	1	0.631482	-6373.8	4.848	14.768	-3.114	17.882
(no SPH)	1	1	0.634529	-5922.1	4.596	14.005	-3.810	17.815
	0	2	0.635542	-5772.0	4.518	13.752	-4.031	17.783
Diffusion SPH	0	1	0.674382	-13.4	0.510	0.662	-1.043	1.705
	1	1	0.674384	-13.0	0.617	0.693	-1.133	1.826
	0	2	0.674395	-11.5	0.660	0.701	-1.15	1.851

Table 11
Integral parameters for the TREAT 3 × 3 with SPH corrected diffusion (h1p1).

Solver	Source	Absorption	Leakage	Flux
Ref. Void	2.2379e+14	2.1852e+14	5.2646e+12	9.0420e+16
Ref. Refl.	2.2301e+14	2.2300e+14	0.0000e+00	9.2047e+16
SPH Void	2.2292e+14	2.1838e+14	5.0063e+12	9.0259e+16
SPH Refl.	2.2301e+14	2.2300e+14	0.0000e+00	9.2041e+16
% rel. diff. Void	−0.389	−0.064	−4.905	−0.177
% rel. diff. Refl	−0.002	−0.004	0.000	−0.007

Table 12
Comparison of solution algorithms for the TREAT 3 × 3 supercell with diffusion.

Algorithm	h	p	free iter.	SPH iter.	total iter.	ϵ_μ	CPU	speedup
traditional	0	1	–	358	358	3.115e−6	126.6	–
PJFNK	0	1	5	5	10	3.115e−6	22.0	5.76
traditional	1	1	–	298	298	1.379e−8	366.6	–
PJFNK	1	1	5	6	11	1.379e−8	67.1	5.47
traditional	0	2	–	364	364	7.829e−8	851.5	–
PJFNK	0	2	5	6	11	7.829e−8	87.86	9.69

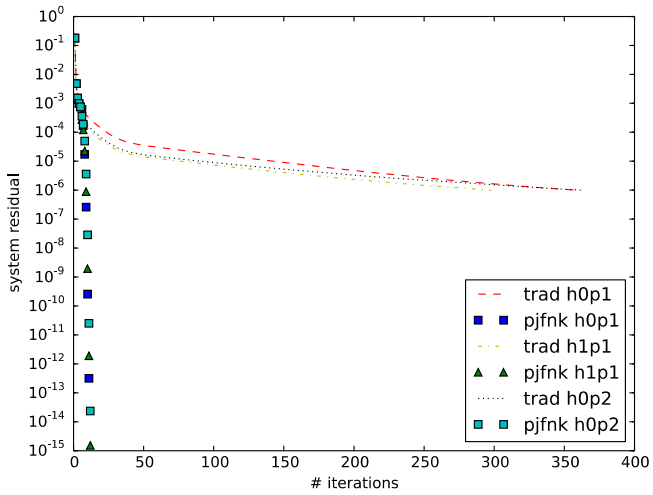

Fig. 8. Convergence of the traditional and PJFNK SPH algorithms for the diffusion operator.

condition. This fact is confirmed with a set of similar runs with reflected boundary conditions, which are shown in Table 10. Similar patterns in the spatial convergence of the SPH correction emerge from the reflected cases and even though the eigenvalues are now within ∼12 pcm of the reference, the powers are slightly worse. Further analyzing the integral reaction rates in Table 11 reveals that the inconsistency in the eigenvalues mainly arises from error in the source rate when applying void boundary conditions.

A comparison of the traditional and PJFNK-SPH iterative algorithms with various spatial discretizations is shown in Table 12. Similarly to the LWR assembly case, speedups of 5–10 times are observed for diffusion. Due to the presence of the void boundary condition, it is necessary to improve the initial guess for the PJFNK-SPH by performing *free SPH iterations*. Five *free SPH iterations* are enough to guarantee convergence of the solution for the PJFNK-SPH. The convergence tolerance of the SPH factors (ϵ_μ) is included for illustration purposes. A plot of the system residual versus number of iterations is included in Fig. 8; note that the MOOSE based PJFNK system tests the convergence on the residual vector and not the relative change from one iteration to the next as illustrated in Algorithm 2. The plot clearly illustrates the slow convergence rates for the traditional Picard iterations versus the high convergence rate of PJFNK-SPH.

A number of spatial and angular convergence studies were conducted with the P_N and S_N transport solvers which lead to similar improvements to those observed with the diffusion operator. The results form the highest angular order employed are shown in Tables 13 and 14, respectively. The scattering order was fixed to linearly anisotropic scattering, since no sources of high order scattering exist in this problem. The solution with the best spatial and angular convergence is obtained with S_6 using a second order Lagrange representation and leads to a difference of ∼202 pcm with and rms error of 0.674%. This rms error is higher than diffusion, but this is a better converged solution and a similar pattern emerges, whereby the power metrics slightly deteriorate with better convergence.

The SPH procedure could not be converged for transport solutions with the traditional SPH algorithm. Convergence of the PJFNK-SPH algorithm with the coarse spatial mesh was attained using a damped Newton Method because using *free SPH iterations* was not effective in this case. The convergence of the undamped PJFNK-SPH with *free SPH iterations* is restored when refining the spatial mesh. Fig. 9 includes the convergence behavior of the various approaches. Three unconverged cases are included: 1) PJFNK-SPH with no *free SPH iterations* (*nofree*), 2) PJFNK-SPH with *free SPH iterations*, which gives the same results as the traditional SPH algorithm (*wfree*) and 3) PJFNK-SPH with a damping factor of 0.5 (*alpha = 0.5*). The converged cases with damped PJFNK-SPH (alpha = 0.3, 0.4, 0.45) show a worse convergence rate than that observed with the diffusion operator and are typical of damped systems. The number of iterations and run times for the P_N solver with various spatial convergences are displayed in Table 15.

The use of *free SPH iterations* leads to an additional optimization problem, since it is not clear how many *free SPH iterations* lead to the fastest convergence path. This is reported in Table 16 and Fig. 10. The optimal number of iterations for the P_1 solver and h1p1 refinement is near 10, but that can be misleading since doing less iterations does not guarantee a faster convergence as proven with the cases using 3 and 5 iterations. The importance of the

Table 13
P_N solutions for the TREAT 3 × 3 supercell (l = 1).

Discretization	h	p	Eigenvalue	pcm	rms	max	min	range
ref	–	–	0.67320	–	–	–	–	–
P_5	0	1	0.64293	−4495.4	3.646	10.962	−2.052	13.014
(no SPH)	1	1	0.64670	−3935.5	3.331	10.003	−2.603	12.606
	0	2	0.64792	−3754.5	3.237	9.696	−2.78	12.476
P_5 SPH	0	1	0.67542	330.8	0.412	0.649	−1.162	1.811
	1	1	0.67510	282.0	0.637	0.609	−1.726	2.335
	0	2	0.67501	269.1	0.716	0.756	−1.878	2.634

Table 14
S_N solutions for the TREAT 3 × 3 supercell (l = 1).

Discretization	h	p	Eigenvalue	pcm	rms	max	min	range
ref	–	–	0.67320	–	–	–	–	–
S_6	0	1	0.64292	−4496.7	3.646	10.964	−2.04	13.004
(no SPH)	1	1	0.64675	−3928.3	3.322	9.99	−2.565	12.555
	0	2	0.64796	−3748.2	3.23	9.683	−2.751	12.434
S_6 SPH	0	1	0.67500	267.6	0.395	0.617	−1.071	1.688
	1	1	0.67465	215.6	0.602	0.715	−1.626	2.341
	0	2	0.67455	201.6	0.674	0.838	−1.772	2.61

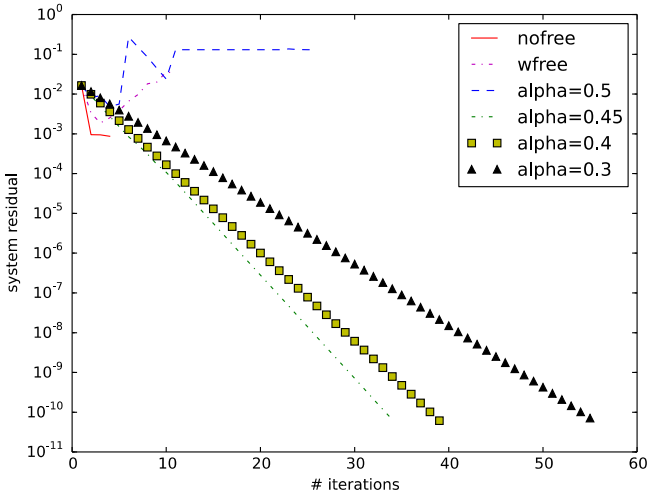

Fig. 9. Convergence of the pjfnk-SPH solver for the P_1 operator (h0p1).

initial guess for the PJFNK-SPH cannot be overstated. The plot also illustrates the lack of convergence of the traditional Picard iteration and the high convergence rate that follows when the PJFNK, without dampers, takes over.

The effects of the SPH correction on the power distribution are included in Fig. 11. The diffusion solution and the difference between diffusion and SPH-diffusion are shown in Figs. 11(a) and 11(b), respectively. As observed previously, the power is overestimated in the control rod element, probably due to large error in the absorption for the diffusion operator, and underestimated in the standard fuel elements.

4.3.1. Coupled test reactor

The base model could not be converged with any SPH algorithm, possibly due to the existence of large gradients in the spatial solution, so further spatial discretization was necessary. The reference eigenvalue is 1.14585 ± 0.97 pcm and the cross section library includes quartic order scattering matrices.

The results from eigenvalue calculations are shown in Tables 17 and 18 with one uniform h-refinement (h1p1) and one p-refinement (h0p2), respectively. Diffusion appears to produce better eigenvalues and power estimates compared to the P_N transport solutions, but this is likely due to poor convergence and cancellation of error. This is apparent in the range of the % rel. diff. of the power distribution, which indicates that the P_N solutions are better converged. Furthermore the P_3 and P_5 solutions show consistency in the extrema for various regions of the core, underpredicting the thermal and overpredicting the fast region. In contrast, diffusion and P_1 exhibit a positive maximum and a negative minimum.

Table 16
P_1 Convergence with *free SPH iterations* (h1p1).

free iter.	SPH iter.	total iter.	time
3	10	13	257.9
5	15	20	394.0
10	5	15	225.0
15	7	22	307.9

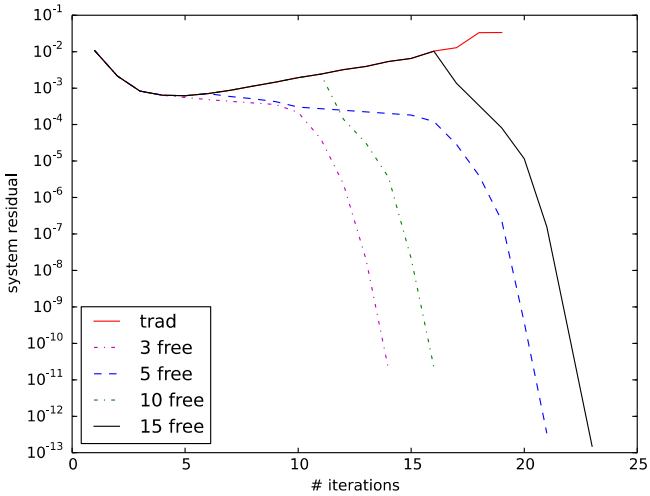

Fig. 10. Convergence of the PJFNK-SPH solver for the P_1 operator (h1p1).

When any solution is further discretized with h0p2, the eigenvalue difference and the power RMS increase while the power range narrows. A strong dependence in the angular convergence is observed in the P_N solvers which overestimate the eigenvalue ~700 pcm beyond the 434 pcm from diffusion.

The SPH-corrected results are included in Tables 19 and 20 and show a strong dependence on spatial and angular discretization. The solutions with the h1p1 are within 160 pcm of the reference, with RMS powers near 0.5%. In particular, the solution with higher order P_N transport drops to ~117 from 1,100 pcm. Further discretization with h0p2 leads to almost one order of magnitude improvement in the eigenvalue difference and halving of the RMS difference for P_3 and P_5.

The dependence of the SPH correction on the scattering order is very weak and linear anisotropic scattering is sufficient to obtain good solutions (Table 21).

The performance metrics for this problem in Table 22 show that the P_3 and P_5 solutions could not be converged with the traditional Picard iterative process, but PJFNK-SPH was able to converge in all cases. The speedups for Diffusion are lower than in the other reactor types, but a factor of 6 is obtained for the P1 equations.

Table 15
PJFNK-SPH convergence for the TREAT 3 × 3 supercell with P_N.

	h	p	free iter.	SPH iter.	total iter.	ϵ	CPU
P_1 SPH	0	1	0	29	29*	5.4679e−6	82.1
	1	1	10	6	16	1.0801e−6	248.0
	0	2	10	6	16	4.5040e−6	386.7
P_3 SPH	0	1	0	26	26*	2.0845e−6	222.5
	1	1	10	6	16	3.1199e−6	1449.8
	0	2	10	6	16	6.9544e−6	2175.7
P_5 SPH	0	1	0	26	26*	3.2287e−6	607.6
	1	1	10	6	16	3.2141e−6	5533.3
	0	2	10	6	16	7.0243e−6	6718.4

* Newton damping.

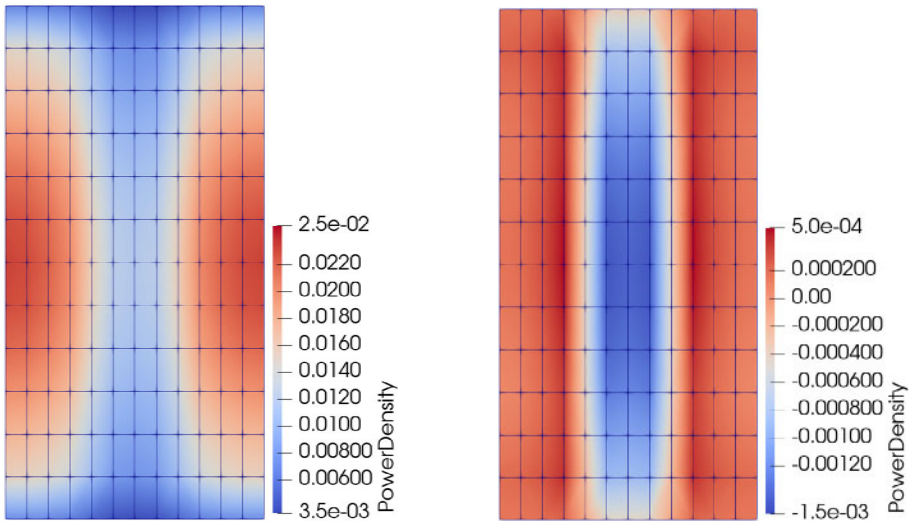

(a) Diffusion values (b) SPH-correction

Fig. 11. SPH-correction of the power density in the TREAT supercell (h0p1).

Table 17
Coupled Tests Reactor results with h1p1 discretization.

Discretization	pcm	region	rms	max	min	range
Diffusion	407.2	thermal	1.098	1.251	−1.603	2.854
(no SPH)		fast	0.511	1.016	−0.658	1.674
P_1	494.3	thermal	1.157	0.915	−1.861	2.776
(no SPH)		fast	0.635	1.185	−0.236	1.421
P_3	1057.5	thermal	2.522	−2.228	−2.789	0.561
(no SPH)		fast	2.576	2.950	1.936	1.014
P_5	1103.5	thermal	2.483	−2.273	−2.683	0.410
(no SPH)		fast	2.527	2.859	2.013	0.846

Table 18
Coupled Tests Reactor results with h0p2 discretization.

Discretization	pcm	region	rms	max	min	range
Diffusion	434.9	thermal	1.028	0.897	−1.618	2.516
(no SPH)		fast	0.525	0.894	−0.379	1.273
P_1	514.3	thermal	1.140	0.586	−1.872	2.458
(no SPH)		fast	0.720	1.061	0.022	1.083
P_3	1076.4	thermal	2.728	−2.277	−2.948	0.671
(no SPH)		fast	2.802	3.210	1.874	1.336
P_5	1123.4	thermal	2.684	−2.421	−2.836	0.415
(no SPH)		fast	2.745	3.112	1.952	1.160

Table 19
Coupled Tests Reactor SPH-corrected results with h1p1 discretization.

Discretization	pcm	region	rms	max	min	range
Diffusion SPH	160.2	thermal	0.552	0.725	0.381	0.344
		fast	0.569	−0.325	−0.658	0.334
P_1 SPH	156.8	thermal	0.637	0.994	0.297	0.697
		fast	0.622	−0.373	−0.714	0.340
P_3 SPH	116.9	thermal	0.514	0.862	0.186	0.677
		fast	0.493	−0.298	−0.565	0.267
P_5 SPH	116.8	thermal	0.521	0.914	0.157	0.757
		fast	0.495	−0.300	−0.566	0.266

Table 20
Coupled Tests Reactor SPH-corrected results with h0p2 discretization.

Discretization	pcm	region	rms	max	min	range
Diffusion SPH	-12.9	thermal	0.347	−0.236	−0.459	0.223
		fast	0.356	0.410	0.217	0.192
P_1 SPH	34.2	thermal	0.129	0.053	−0.290	0.343
		fast	0.090	0.097	0.078	0.019
P_3 SPH	1.3	thermal	0.219	0.001	−0.447	0.448
		fast	0.192	0.219	0.127	0.092
P_5 SPH	1.5	thermal	0.205	−0.046	−0.371	0.325
		fast	0.190	0.216	0.126	0.090

Table 21
Scattering order dependence of the SPH in the CTR with P_5.

Scattering order	pcm	region	rms	max	min	range
1	1.1	thermal	0.206	−0.045	−0.376	0.331
		fast	0.191	0.217	0.126	0.091
2	2.6	thermal	0.209	−0.018	−0.410	0.393
		fast	0.188	0.214	0.124	0.091
4	1.5	thermal	0.205	−0.046	−0.371	0.325
		fast	0.190	0.216	0.126	0.090

Table 22
PJFNK-SPH convergence for the CTR (h0p2).

discretization	SPH solver	free iter.	SPH iter.	total. iter.	ϵ_μ	CPU	speedup
Diffusion SPH	trad.	–	54	54	3.46E−06	45.1	
	pjfnk	5	5	10	3.46E−06	29.1	1.55
P_1 SPH	trad.	–	436	436	9.57E−07	965.7	
	pjfnk	20	5	25	9.57E−07	156.2	6.2
P_3 SPH	trad.	–	nc	nc	–	–	
	pjfnk	20	5	25	–	1381.3	–
P_5 SPH	trad.	–	nc	nc	–	–	
	pjfnk	20	5	25	–	5545.0	–

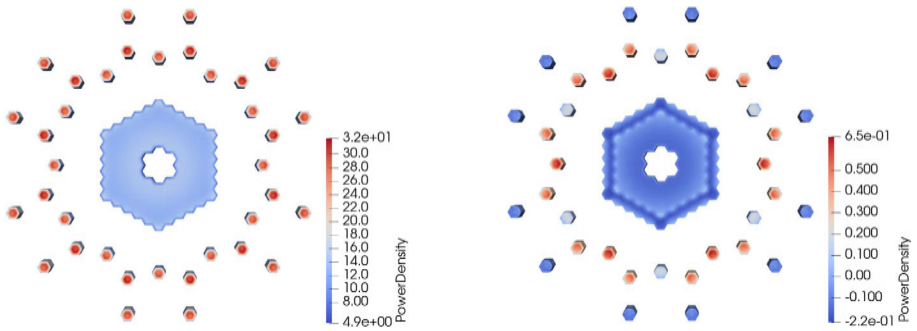

(a) Diffusion values (b) SPH-correction

Fig. 12. SPH-correction of the power density in the CTR (h1p1).

The effects of the SPH correction on the power distribution are included in Fig. 12 with 12(a) showing the diffusion solution and 12(b) showing the difference between the diffusion and the SPH-corrected diffusion solution. The SPH corrections to the power distribution are small in the fast regions and outer reflector thermal blocks. The largest corrections occur in the thermal blocks that are closest to the neutron filters.

5. Conclusion

The analysis of various reactor types and configurations has shown the efficacy of employing a Newton method in the solution of the SPH nonlinear system of equation in a CFEM discretization. The Newton method, with a proper initial guess, yields a very high convergence rate for the SPH iteration with diffusion and transport

in closed geometries with reflector regions, where historically the traditional SPH method failed to converge at all. Additionally, a variety of tools are included in MOOSE via PETSc to help converge difficult problems. Newton damping is employed in one particular case to constrain the extrapolation in the Newton method. Other times, in the presence of void boundary conditions and reflectors, it was necessary to improve the initial guess by performing free SPH iterations with a Picard iterative process to bring the solution vector within the radius of convergence of the Newton method. The increase in the solution speed between the traditional SPH and the PJFNK-SPH is significant. The solution time is decreased by a factor of 5 for diffusion and 10–15 for transport in the problems analyzed. The speedup should increase with the size and complexity of the nonlinear problem.

This work reveals that the PJFNK-SPH method performs very well and dramatically improves the eigenvalues and reaction rates. The SPH-corrected cross sections yield eigenvalues that are near exact relative to the reference solution for reflected geometries, even with reflector regions. In void geometries, the accuracy of SPH corrected cross sections is problem dependent and eigenvalue differences can be within a few to a few hundred pcm, but still preserving the accuracy in the power distribution. The root-mean-square of the percent relative difference in the power distribution is below 0.8% of the reference Monte Carlo solution in all instances of water-moderated, graphite-moderated and fast reactor types.

Furthermore, the formalism to perform the SPH-correction on the transport equation was also introduced and tested. The problems analyzed exhibit little benefit from SPH-corrected transport compared to SPH-corrected diffusion for typical scoping calculations, but for more detailed analysis it can yield superior convergence of the solution, specifically in the case of the coupled fast-thermal reactor.

Yet the question remains on how SPH corrections affect transient behavior, since the method does not guarantee the conservation of the neutron current. Nevertheless, this initial implementation produced a robust nonlinear SPH solver that can be further improved in order to achieve better estimates of the neutron current with a CFEM discretization, which will be the focus of future research.

Acknowledgements

This work was supported by the U.S. Department of Energy, Office of Nuclear Energy, Advanced Modeling and Simulation Program, under DOE-NE Idaho Operations Office Contract DEAC07-05ID14517.

References

Berry, R.A., Peterson, J.W., et al., 2014. RELAP-7 theory manual, Tech. rep. Idaho National Laboratory.

Chiba, G., Tsuji, M., Sugiyama, K., Narabayashi, T., 2012. A note on application of superhomogénéisation factors to integro-differential neutron transport equations. Nucl. Sci. Technol. 49 (2), 272–280.

Fujita, T., Endo, T., Yamamoto, A., 2015. Application of correction technique using leakage index combined with SPH or discontinuity factors for energy collapsing on pin-by-pin BWR core analysis. Nucl. Sci. Technol. 52 (3), 355–370.

Gaston, D., Newman, C., Hansen, G., Lebrun-Grandié, D., 2009. MOOSE: a parallel computational framework for coupled systems of nonlinear equations. Nucl. Eng. Des. 239 (10), 1768–1778.

Gleicher, F., Ortensi, J., et al., 2014. The coupling of the neutron transport application RATTLESNAKE to the fuels perfomance application BISON. In: International Conference on Reactor Physics (PHYSOR 2014), Kyoto, Japan.

Grundmann, U., Mittag, S., 2011. Super-homogenisation factors in pinwise calculations by the reactor dynamics code dyn3d. Ann. Nucl. Energy 38 (10), 2111–2119.

Guerin, P., Courau, T., Couyras, D., Girardi, E., 2011. Equivalence et correction de transport dans COCAGNE, Tech. rep. EDF - RD.

Hébert, Alain, 1981. Développement de la méthode SPH: Homogénéisation de cellules dans un réseau non uniforme et calcul des paramètres de réflecteur Ph. D. Thesis. CEA-N-2209.

Hébert, A., 1993. A consistent technique for the pin-by-pin homogenization of a pressurized water reactor assembly. Nucl. Sci. Eng. 113 (3), 227–238.

Hébert, A., 2015. A reformulation of the transport-transport SPH equivalence technique, no. 7, 7ICMSNSE.

Hébert, A., Benoist, P., 1991. A consistent technique for the global homogenization of a pressurized water reactor assembly. Nucl. Sci. Eng. 109 (4), 360–372.

Hébert, A., Mathonnière, G., 1993. Development of a third-generation superhomogeneisation method for the homogenization of a pressurized water reactor assembly. Nucl. Sci. Eng. 115 (2), 129–141.

Horelik, N., Herman, B., Forget, B., Smith, K., 2013. Benchmark for evaluation and validation of reactor simulations (BEAVRS). Sun Valley, Idaho.

Kavenoky, A., 1978. The SPH homogenization method, IAEA-TECDOC-231, Lugano.

Knoll, D., Keyes, D., 2004. Jacobian-free Newton-Krylov methods: a survey of approaches and applications. Comput. Phys. 193 (2), 357–397.

Laurier, Alexandre, 2016. Implementation of the SPH Procedure within the MOOSE Finite Element Framework Ph.D. Thesis. École Polytechnique de Montréal.

Leppänen, J., 2015. Serpent - a continuous-energy Monte Carlo reactor physics burnup calculation code, Tech. rep. VTT Technical Research Centre of Finland.

Li, M., Wang, K., Yao, D., 2014. The super equivalence method in Monte Carlo based homogenization, no. 22, In: Proceedings of the 2014 22nd International Conference on Nuclear Engineering, ICONE22.

Ma, J., Wang, G., Yuan, S., Huang, H., Qian, D., 2015. An improved assembly homogenization approach for plate-type research reactor. Ann. Nucl. Energy 85, 1003–1013.

Nikitin, E., Fridman, E., Mikityuk, K., 2015. On the use of the SPH method in nodal diffusion analyses of SFR cores. Ann. Nucl. Energy 85, 544–551.

Ortensi, J., et al., 2016. Preparation of a neutron transport data set for simulations of the transient test reactor facility. In: PHYSOR-2016, ANS Topical Meeting on Reactor Physics, Sun Valley, Idaho, USA.

Smith, K., 1986. Assembly homogenization techniques for light water reactor analysis. Prog. Nucl. Energy 17 (3), 303–335.

Wang, Y., 2013. Nonlinear diffusion acceleration for the multigroup transport equation discretized with S_N and continuous FEM with RATTLESNAKE. In: Proceedings to the International Conference on Mathematics, Computational Methods & Reactor Physics (M&C 2013), Sun Valley, Idaho, USA.

Williamson, R. et al., 2012. Multidimensional multi-physics simulations of nuclear fuel behaviour. Nucl. Mater. 423, 149–163.

Yamamoto, A., Tatsumi, M., Kitamura, Y., Yamane, Y., 2004. Improvement of the SPH method for pin-by-pin core calculations. Nucl. Sci. Technol. 41 (12), 1155–1165.

Youinou, G., Sen, S., et al., 2016. A Versatile Coupled Thermal-Fast Irradiation Test Reactor. In: International Conference on Reactor Physics (PHYSOR 2016), Sun Valley, Idaho, U.S.A.